

Towards Accurate Thermal Property Predictions in Uranium Nitride using Machine Learning Interatomic Potential

Beihan Chen,¹ Zilong Hua,² Jennifer K. Watkins,² Linu Malakkal,² Marat Khafizov,³ David H. Hurley,² and Miaomiao Jin^{1, a)}

¹*Department of Nuclear Engineering, The Pennsylvania State University, University Park, PA 16802, USA*

²*Idaho National Laboratory, Idaho Falls, ID 83415, USA*

³*Department of Mechanical and Aerospace Engineering, The Ohio State University, Columbus, OH 43210, USA*

We present a combined computational and experimental investigation of the thermal properties of uranium nitride (UN), focusing on the development of a machine learning interatomic potential (MLIP) using the moment tensor potential (MTP) framework. The MLIP was trained on density functional theory (DFT) data and validated against various quantities including energies, forces, elastic constants, phonon dispersion, and defect formation energies, achieving excellent agreement with DFT calculations, prior experimental results and our thermal conductivity measurement. The potential was then employed in molecular dynamics (MD) simulations to predict key thermal properties such as melting point, thermal expansion, specific heat, and thermal conductivity. To further assess model accuracy, we fabricated a UN sample and performed new thermal conductivity measurements representative of single-crystal properties, which show strong agreement with the MLIP predictions. This work confirms the reliability and predictive capability of the developed potential for determining the thermal properties of UN.

Keywords: Uranium Nitride, Thermal property, Phonon, Machine learning interatomic potential

^{a)}Electronic mail: mmjin@psu.edu

I. INTRODUCTION

In comparison to the traditional uranium oxide nuclear fuel, uranium nitride (UN) fuel offers several benefits, including higher fissile density, higher thermal conductivity¹, good compatibility with the PUREX process², and good compatibility with most cladding materials, resulting in an extended fuel cycle time³. Due to these advantages, UN is considered a strong candidate for long-term accident-tolerant fuel in light water reactors and a promising option for Generation IV nuclear reactors⁴. Therefore, it is essential to understand the thermal behavior of UN. Several properties of UN, such as phonon dispersion⁵, elastic constants^{6,7}, thermal expansion⁸, specific heat capacity⁹, and thermal conductivity^{1,10}, have been investigated experimentally and summarized by Hayes et al.^{1,7,11,12} and more recently by Miller et al.¹³. In addition to experimental measurements, atomic scale modeling such as density functional theory (DFT) and molecular dynamics (MD) plays a crucial role in interpreting and complementing existing experimental data of UN properties.

As one of the most accurate quantum mechanical calculation methods of materials modeling, DFT has been widely used to investigate physical properties of UN^{14–18}. However, it requires global self-consistent convergence of the electronic structure, whose computational cost is $O(N^3)$, thereby constraining the feasible system size to a range of $N=10-100$ atoms^{19,20}. Compared to DFT, MD simulations offer a scalable approach for evaluating thermal properties at finite temperatures and larger length scales, overcoming the common size effects expected in DFT calculations¹⁹. However, the predictive capability of MD simulations critically depends on the quality of the interatomic potential. Over the years, several empirical interatomic potentials have been developed for UN. Kurosaki et al.^{21,22} constructed a Busing–Ida-type potential augmented by a Morse function to study properties such as thermal expansion, specific heat capacity and thermal conductivity. Chen et al.²³ developed another Morse-type potential to calculate the structural and elastic properties of UN. However, Morse potentials lack the ability to represent directional bonding, limiting their accuracy for UN²⁴. To address this limitation, an angular-dependent potential (ADP) was developed by Kuksin et al.²⁵ using force-matching technique to investigate the diffusion of point defects. This ADP was later modified by Tseplyaev and Starikov²⁶ to improve the accuracy of UN property descriptions at high pressures. Additionally, a many-bodied embedded-atom (EAM) potential combined with a pairwise Buckingham term for UN was developed by Kocevski et al.²⁷ to investigate the elastic properties, specific heat capacity and Xenon diffusion in UN. Most recently, AbdulHameed et al.²⁸ assessed the performance of Tseplyaev and Starikov’s

ADP (hereafter referred to as the Tseplyaev potential)²⁶ and Kocevski et al.'s EAM (hereafter referred to as the Kocevski potential)²⁷ by comparing derived quantities, including UN thermal expansion, melting point, elastic properties, specific heat capacity, phonon properties and defect formation energies. They showed that the Tseplyaev potential excels in capturing the energetic aspects of UN, whereas the Kocevski potential performs better in modeling the structural properties. Given the differences among available interatomic potentials, a reliable potential is still desired that can ideally capture all these properties for predicative modeling of UN.

In recent years, machine learned interatomic potentials (MLIPs) have emerged as an effective alternative for developing quantum-accurate interatomic models. Developing an MLIP requires generating a diverse dataset of atomic configurations with corresponding energies, forces, and stresses from DFT calculations, which is then used to train the potential using a specific machine learning framework. A variety of MLIP training approaches have been proposed, such as the neural-network potential (NNP)^{29,30}, the Gaussian approximation potential (GAP)^{31,32}, the spectral neighbor analysis potential (SNAP)^{20,33}, and the moment tensor potential (MTP)³⁴. Among these, the MTP framework has demonstrated an excellent trade-off between accuracy and computational efficiency³⁵. Moreover, it has been successfully applied to predict the thermal properties in metal nitrides³⁶. Building on these advantages, we developed an MTP for UN based on a DFT-generated dataset. While a recent ML potential³⁷ has been developed using a hierarchically interacting particle neural network (hereafter referred to as HIP-NN potential) and applied to predict the general properties of UN, its application to thermal modeling remains unclear. In this work, we specifically target the accurate prediction of bulk thermal conductivity in UN by combining the developed MTP with MD simulations and the relaxation time approximation (RTA) of the Boltzmann transport equation (BTE) for thermal conductivity calculation. Note that for materials with a wide phonon band gap like UN, at high temperatures, the RTA approach requires an evaluation of higher-order interatomic force constants (IFCs, up to the fourth order), which traditionally necessitates computationally expensive DFT calculations for thousands of supercell structures based on the frozen phonon method³⁸. By substituting DFT with an accurate MTP, we enable the use of larger supercells and significantly reduce the computational cost, thereby enhancing the prediction capability of thermal conductivity comparing to experimental data. Moreover, the developed MTP also enables MD prediction of other thermal properties, such as melting point, thermal expansion, and specific heat, and the results show strong agreement with experimental measurements, further validating the reliability of the developed potential for evaluating thermal properties.

II. METHODS

A. Moment tensor potential

Moment tensor potential (MTP) is a local potential that describes a system based on moment tensor descriptors of the atomic environment in the system³⁴. The potential energy of an atomic system described by MTP is defined as a sum of the energies of atomic environments of the individual atoms,

$$E_{\text{MTP}} = \sum_i V(n_i) \quad (1)$$

where n_i stands for the local environment of atom i and $V(n_i)$ represents its corresponding atomic energy contribution. The local environment is described by a set of structural descriptors that encode the relative positions of neighboring atoms within a cutoff sphere centered on the atom of interest. Theoretically, any continuous function describing local environments can be approximated by linear combinations of polynomial basis functions \mathbf{B}_α

$$V_i = \sum_\alpha \xi_\alpha \mathbf{B}_\alpha \quad (2)$$

The coefficient ξ_α corresponding to the basis function \mathbf{B}_α are optimized during the ML training process by fitting to the reference dataset. Once the convergence criterion is satisfied, the training is completed, and the interatomic potential is constructed.

B. ML training procedure

For the generation of training set, all DFT calculations were performed using the Vienna *ab initio* simulation package (VASP 6.4.1)^{39,40}. The results presented were obtained using the generalized gradient approximation (GGA) functional for exchange correlation within the Perdew-Burke-Ernzerhof (PBE) form⁴¹.

In previous works, Hubbard U correction^{42,43} has been applied to better account for the correlated nature of uranium's 5f electrons. However, the¹⁶ systematic assessment of DFT for UN by Kocevski et al.¹⁶ hints that the use of Hubbard U correction causes instability and results in a poorer agreement with experiments, particularly when antiferromagnetic (AFM) ordering of the uranium spins is applied. In contrast, ferromagnetic (FM) ordering (as shown in Fig. 1a),

combined with spin-orbit coupling (SOC), yields better agreement with experimental data without the use of Hubbard U. Experiments have shown that U atoms in UN exhibit AFM ordering below the Néel temperature 53K⁴⁴ and FM ordering above 53 K. In this work, the temperature range investigated is above 77 K; therefore, FM ordering with spin-orbit coupling (SOC) is employed in the DFT calculations. A $2 \times 2 \times 2$ UN supercell was employed, with a plane-wave energy cutoff of 520 eV and Gaussian smearing applied with a 0.05 eV smearing width. Energy convergence criteria was set to 10^{-4} eV, and a $3 \times 3 \times 3$ K-point mesh was employed for Brillouin zone sampling which has been verified to be sufficiently accurate (see Supplementary Materials (SM), Figure S1 and S2 for the convergence test).

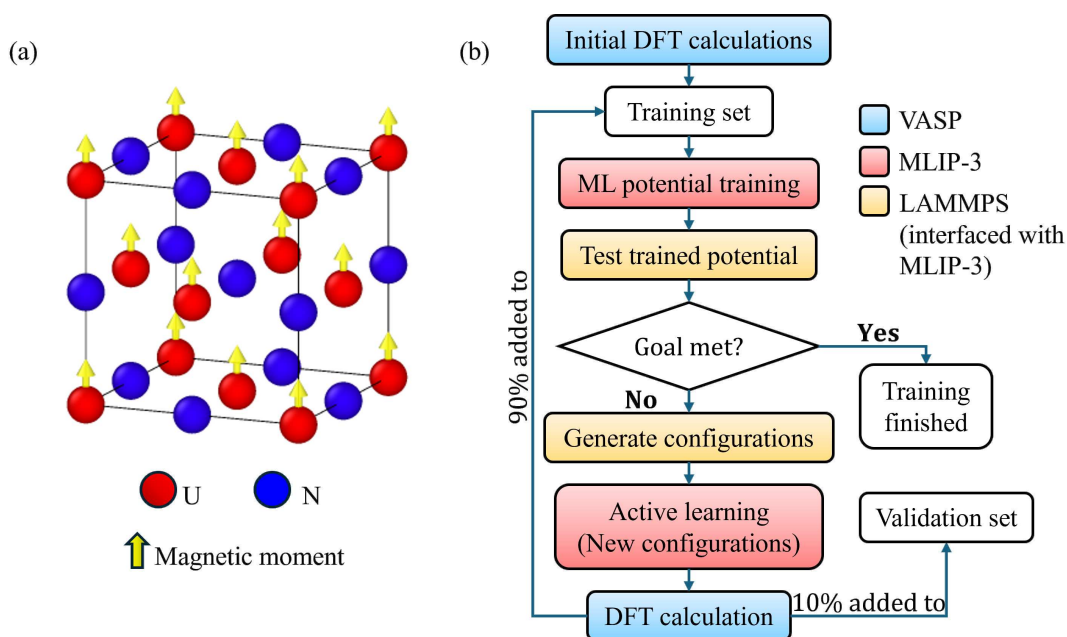


Figure 1. (a) Model of FM ordering of the spins of uranium atom. (b) Flowchart of the MLIP training procedure.

The overall ML training workflow is illustrated in Fig.1b. It begins with the generation of an initial training dataset from DFT calculations, which provide energies, forces, and stress tensors for a set of representative atomic configurations with different atomic displacements and lattice parameters. This dataset is used to train an initial MTP, and the developed MTP is then applied in MD simulations to predict energies and forces for various UN configurations. If the accuracy is insufficient, the MTP is used to generate new configurations via MD, and an active learning algorithm^{45,46} selects representative structures to expand the training dataset and improve its diversity. DFT calculations are then performed on the selected configurations. The resulting data are

randomly divided into a training set (90%) and a validation set (10%). A new MTP is subsequently refitted based on the previous MTP and the updated training set. This iterative process continues until the MTP reaches the target accuracy. The final dataset contains 3236 atomic configurations. This workflow is enabled by the MLIP-3 package⁴⁶, which constructs the MTP based on DFT-derived atomic configurations. The LAMMPS simulation package⁴⁷, interfaced with MLIP-3 via the LAMMPS-MLIP-3 plugin⁴⁸, is employed to integrate the trained potential into MD simulations.

C. Property evaluation

1. Physical properties

A. Equation of state (EOS)

Strains were applied in the x, y, and z directions of a $2 \times 2 \times 2$ UN conventional supercell. The potential energies of the strained structures were calculated using both MD with the developed MTP and DFT employing the same settings used in database generation. The lattice constants were determined by fitting of the energy-volume curves from both MTP and DFT using the Birch-Murnaghan model⁴⁹.

B. Elastic constants

The cubic crystal structure of UN has only three independent elastic constants: C_{11} , C_{12} , and C_{44} . These constants were calculated using the energy-strain method^{50,51} based on a set of three equations. Starting from the equilibrium structure obtained from the EOS, strains were applied simultaneously along $\pm x$, $\pm y$, and $\pm z$; along $\pm x$ and $\pm y$; and in the $\pm xy$ shear direction. The resulting energy-volume curves were then fitted to the corresponding equations to extract the elastic constants.

C. Phonon dispersion

We performed phonon dispersion calculations using the Phonopy package⁵², which employs the finite displacement method to compute second-order force constants⁵³. These calculations were conducted for both MTP and DFT, utilizing a $10 \times 10 \times 10$ k-point mesh to sample the Brillouin zone. The results were then compared to validate the accuracy of the MTP predictions.

D. Defect formation energies

To facilitate comparison with previous studies, the formation energy E_f of stoichiometric defects in UN, including Frenkel pairs (FPs) and Schottky defects (SDs), was predicted by MD calculations enabled by the developed MTP, with validation from DFT calculations. Both bound and unbound configurations were considered for uranium FP (U_{FP}) and nitrogen FP (N_{FP}) and Schottky defects. The formation energies are computed using the following expressions:

$$\begin{aligned} E_f(\text{FP}) &= E_d - E_p \\ E_f(\text{SD}) &= E_d - \frac{N-2}{N} E_p \end{aligned} \quad (3)$$

where N is the total number of atoms in the perfect supercell, E_p is its total energy, and E_d is the potential energy of the defect-bearing supercell of the same size. All calculations are performed using the $2 \times 2 \times 2$ conventional supercell of UN. Individual point defect is generated by removing or inserting U/N into the initially perfect cell. Bound configurations (FP or SD) are constructed by introducing both defects (a vacancy and an interstitial, or two vacancies) within a single supercell, whereas unbound configurations place the defects in separate supercells to simulate spatial separation.

2. *Thermal properties*

A. *Thermal expansion*

For thermal expansion, we computed the relative linear thermal expansion (rLTE), defined as,

$$\text{rLTE} = \frac{a(T) - a_{300}}{a_{300}} \quad (4)$$

where T is the temperature in Kelvin, $a(T)$ is the equilibrium lattice parameter at temperature T , and a_{300} denotes the lattice parameter at 300 K.

To determine $a(T)$, MD simulations were conducted in the isothermal-isobaric (NPT) ensemble using a Nosé–Hoover thermostat and barostat^{54,55} to control temperature and pressure. Each simulation used a conventional $8 \times 8 \times 8$ supercell (See SM Figure S3 and S4 for the convergence test on supercell size) of the UN unit cell, comprising 4096 atoms, and was run at zero external pressure over a temperature range from 300 K to 1800 K in increments of 50 K. For each temperature, the system was equilibrated for 20 ps and the box dimensions were recorded every 1 ps. The average lattice parameter at each temperature was obtained by averaging the box dimensions. A timestep of 1.0 fs was used for all simulations in this work. The calculated $a(T)$ values were then used in Eq. 4 to determine rLTE.

B. Melting point

The $8 \times 8 \times 8$ UN conventional supercell was also used for the calculation of melting point. The system was equilibrated under the NPT ensemble with the temperature ramped from 2600 K to 3600 K and isotropic pressure maintained at zero external pressure using a Nose–Hoover thermostat and barostat. A timestep of 1 fs was used throughout the simulation. Enthalpy was computed during the run and averaged every 4 ps, and the entire simulation was carried out over 200 ps.

C. Specific heat

The specific heat C_p of UN is calculated by

$$C_p = \frac{\partial H}{\partial T} \quad (5)$$

where H is the enthalpy of system converted to J/mol. The MD simulations for specific heat followed the same setup as those used for thermal expansion, with an extend temperature range from 250 K to 1850 K in increments of 50 K. For each temperature, the enthalpy of the system was obtained by averaging over a 20 ps NPT simulation, with data collected at 1 ps intervals. The specific heat was then calculated over the range of 300 K to 1800 K using Eq. 5.

D. Thermal conductivity (Computation)

The total thermal conductivity κ of UN consists of both lattice thermal conductivity (κ_L) and electronic thermal conductivity (κ_e), i.e., $\kappa_{\text{total}} = \kappa_L + \kappa_e$. In this work, κ_L is calculated using the RTA approach,

$$\kappa_L = \Sigma c_V v^2 \tau \quad (6)$$

where c_V is the phonon specific heat at constant volume, v is the phonon group velocity, and τ is the phonon relaxation time, which is evaluated via Matthiessen's rule:

$$\tau^{-1} = \tau_{3\text{ph}}^{-1} + \tau_{4\text{ph}}^{-1} + \tau_{\text{b}}^{-1} + \tau_{\text{iso}}^{-1} + \tau_{\text{elph}}^{-1} \quad (7)$$

where τ^{-1} , the reciprocal of phonon relaxation time, represents phonon scattering rate. $\tau_{3\text{ph}}^{-1}$ and $\tau_{4\text{ph}}^{-1}$ denote the three-phonon and four-phonon scattering rates, respectively, which were calculated using the Phonopy and ShengBTE packages^{56,57} in this work. Forces were calculated with the developed MTP for displaced supercell configurations and the second-, third-, and fourth-order IFCs were extracted based on these configurations and forces. The scalebroad parameter was set

0.5 and mesh was set $30 \times 30 \times 30$ in ShengBTE. A $5 \times 5 \times 5$ primitive UN supercell containing 250 atoms, (see Figure S5 in SM for the convergence test) was used for phonon scattering rates calculation for κ_L . The boundary (τ_b^{-1}) and isotope (τ_{iso}^{-1}) phonon scattering rates are not the primary focus of this work. τ_b^{-1} was computed using ShengBTE's default settings, while τ_{iso}^{-1} was considered using the Tamura model as implemented in ShengBTE. Finally, the electron-phonon scattering rates, τ_{elph}^{-1} , were computed by combining electron data from DFT output of UN and phonon data from the developed MTP using the EPW code^{58,59}. The electron-phonon matrix elements required for the EPW code were initially calculated on a coarse $4 \times 4 \times 4$ q grid, and then interpolated onto fine grids using maximally localized Wannier functions (MLWFs)⁶⁰ construct by random projection method⁶¹ to calculate electron-phonon scattering rates. The obtained τ_{elph}^{-1} were incorporated into the total phonon scattering rates via Matthiessen's rule for thermal conductivity calculations.

κ_e is evaluated using the Wiedemann–Franz law⁶²:

$$\kappa_e = \frac{LT}{\rho} \quad (8)$$

where $L = 2.44 \times 10^{-8} \text{V}^2 \text{K}^{-2}$ is the Lorenz number⁶³, ρ is the electrical resistivity obtained from an empirical single spacing ($\delta = 170 \text{K}$) crystal field (CF) model fitted based on experimental results⁶⁴:

$$\rho(T) = \rho_0 + \rho_{\text{CF}(\infty)} / \cosh^2(\delta/2T) \quad (9)$$

where $\rho_0 = 85.6 \mu\Omega\text{cm}$, $\rho_{\text{CF}(\infty)} = 63.3 \mu\Omega\text{cm}$.

E. Thermal conductivity (Experiment)

The thermal conductivity of UN was obtained by measuring its thermal diffusivity and combining it with literature values of heat capacity and density. For the experimental measurements, a UN sample was prepared using the UN powder feedstock, synthesized via the carbothermic reduction method, received from Los Alamos National Laboratory. The as-received powder was subjected to a high energy ball milling process (300 rpm, 1 hour, Retsch PM 200 planetary ball mill) in a ZrO_2 milling vessel with 5 mm diameter ZrO_2 media and the milled powder was then passed through a 400-mesh ($37 \mu\text{m}$) sieve prior to pressing into pellets of right cylindrical geometry using an automated Carver hydraulic press at $\approx 670 \text{MPa}$ with an 8.25 mm WC die. A small amount of dry zinc stearate (Sprayon MR312) was used as a lubricant on the die surface, die punches, and die faces. All milling and pellet fabrication, and sintering activities occurred in an inert atmosphere

glovebox having under 5 ppm of O₂.

The UN pellets were sintered in a refractory metal sintering furnace (Thermal Technology Model 1100) with pellets placed directly on a tungsten sintering plate within the hot zone of the furnace. A sintering cover gas of oxygen scrubbed Ar/+ 100 ppm N₂ (1 L/min) was used during sintering. The Ar/N₂ mixture is used to avoid UN dissociation and formation of U₂N₃ during the sintering ramp (25 °C/min), at the dwell temperature, 1950°C, for 25 hours, and during the cool-down phase to 1200 °C⁶⁵. Once the sample reached 1200 °C, the atmosphere was switched to UHP Ar for the final cool-down until room temperature to prevent sesquinitride formation.

Thermal diffusivity was measured over the temperature range of 77 K to 300 K, using the spatial-domain thermorefectance (SDTR) technique. In the SDTR system, an intensity-modulated 660-nm continuous wave (CW) laser is used to locally heat up the sample surface and generate the thermal wave (transient temperature variation in both time and spatial domains). The thermal wave propagation in the spatial range of 20 μm is probed by a 532-nm laser through thermorefectance effect. The measurement probing range can be estimated by thermal diffusion length, given by $L_{th} = \sqrt{D/\pi/f}$, where D is the thermal diffusivity and f is the heating laser modulation frequency. In this study, the heating laser is modulated in a frequency range of 20-100KHz, corresponding to thermal diffusion lengths of 4.5-10 μm (assuming $D \approx 6\text{mm}^2/\text{s}$ for UN). As this length scale is significantly smaller than the grain diameter (50-100 μm), the measurements predominantly probe intra-grain heat transport and can be considered representative of single-crystal behavior.

Both the heating and probe laser beams were focused to $\sim 1.5 \mu\text{m}$ -radius spots on the surface of the sample using a 50× objective lens, and the optical power at the sample surface was $\sim 3 \text{ mW}$ and $\sim 0.3 \text{ mW}$ for the heating and probe lasers, respectively. In order to ensure a sufficient thermorefectance response, samples were coated with a thin layer of gold as a transducer⁶⁶. A relatively small thickness ($\sim 30 \text{ nm}$) was selected to reduce the impact of film properties on measurements⁶⁷. Thermal properties of the deposited gold films were determined from co-deposited films of the same thickness on pristine NBK7 substrates. The change of the gold film thermal properties with respect to temperature were considered through an empirical approach⁶⁸. The details of this procedure can be found in previous publications⁶⁹⁻⁷¹.

III. RESULTS AND DISCUSSION

A. MLIP training

The accuracy of the developed MTP was evaluated by comparing its predictions of energies and forces against the DFT reference values in the validation set which includes 450 atomic configurations. The error was quantified via the root-mean-square error (RMSE). As shown in Figures 2a and 2b, the RMSE for MTP-predicted energies and forces relative to DFT values are 2.82 meV/atom and 45.49 meV/Å, respectively. These low RMSE values indicate good agreement between the MTP and DFT calculations. As a reference, Alzate-Vargas et al. obtained 2.48 meV/atom and 111 meV/Å in HIP-NN for UN material³⁷. Hence, this level of accuracy achieved in this study ensures that the MTP is suitable not only for static property predictions (e.g., defect formation energies, elastic constants) but also for temperature-dependent simulations such as thermal transport and thermal expansion.

5

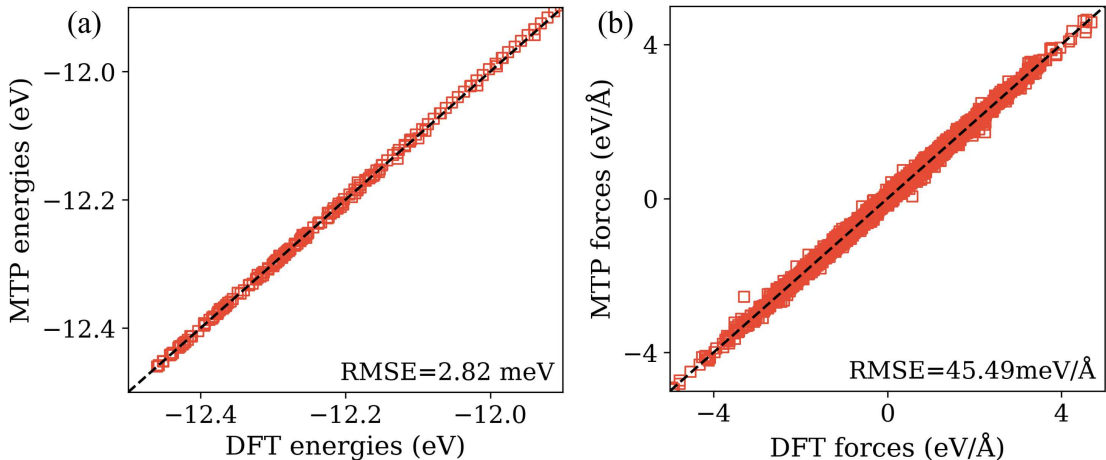


Figure 2. (a) Energies and (b) forces predicted by the developed MTP compared to the DFT reference data in validation set.

B. Physical properties

The equation of state results presented in Fig. 3 compares the energy–volume curves obtained from both MTP and DFT calculations. The two methods yielded very consistent values across the

whole volume range, which implies that the developed MTP accurately captures the underlying cohesive energy landscape of UN. The lattice constants (a_0) extracted from the energy-volume curves in Fig. 3 is listed in Table I and compared with the values from Tseplyaev, Kocevski and HIP-NN potentials^{28,37}. Among all the potentials considered, the lattice constant predicted by the developed MTP shows the closest agreement with the experimental value at 300 K. In contrast, the Tseplyaev potential exhibits a noticeable overestimation of the lattice constant compared to the other potentials.

Accurate prediction of elastic properties is essential for modeling the mechanical behavior of UN under operational and extreme conditions. Starting from the equilibrium structure, the three independent elastic constants C_{11} , C_{12} and C_{44} were calculated from energy-strain method^{50,51}, which used molecular statics calculations of strained supercells to extract those quantities. From these, the Bulk modulus B , Young’s modulus Y and Shear modulus G were derived using the Voigt-Reuss-Hill (VRH) averaging scheme^{72,73}. As summarized in Table I, the MTP-predicted elastic constants and moduli are in good agreement with both experimental data and values from previous studies using other interatomic potentials^{6,7,28,37}.

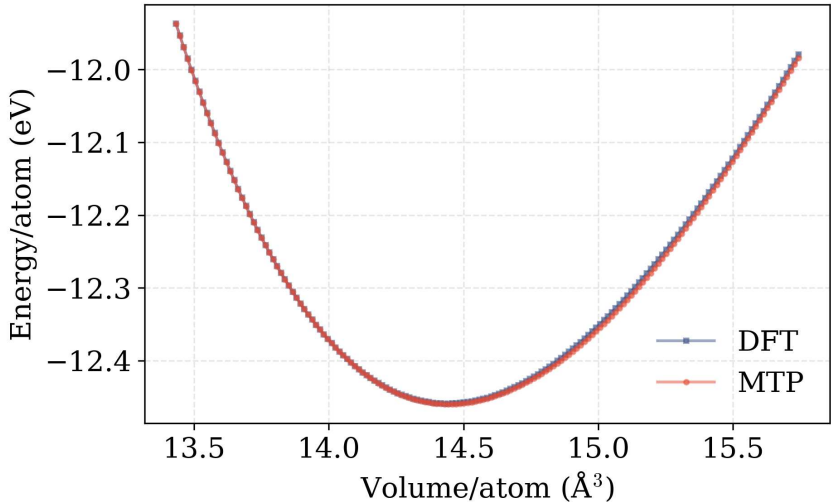


Figure 3. Equation of state predicted by the developed MTP, compared with DFT results calculated using the same settings as those employed for database generation.

We next assessed the ability of the MLIP to capture near-equilibrium vibrational properties by examining the phonon dispersion of UN. Phonons play a key role in thermal transport, particularly in materials with non-negligible contribution to thermal transport via phonons. The phonon dispersion relations calculated using the developed MTP are shown in Figure 4, along with those

	a_0 (Å)	C_{11}	C_{12}	C_{44}	B	E	G
MTP this work	4.87	379.2	111.9	51.2	210.0	205.7	77.5
DFT this work	4.87	390.5	99.7	52.9	196.6	212.33	80.4
Tseplyaev	4.81	586.6	110.5	54.7	269.2	260	105
Kocevski	4.90	425.4	117.0	71.0	219.8	250	95
HIP-NN	4.86*	393	131	43	221		
Experiment	4.88	423.9*	98.1*	75.7*	206.7*	240*	105*

(* at 300 K)

Table I. Lattice constant a_0 (in Å), elastic constants C_{11} , C_{12} , C_{44} , bulk modulus B , Young’s modulus E , and shear modulus G (all in GPa) from the present MTP and DFT calculations, compared with values from the Tseplyaev, Kocevski, and HIP-NN potentials^{28,37}, and experimental data^{6,7,74}.

derived from DFT calculations and experimental data reported by Jackman et al.⁵. Overall, the MTP- and DFT-predicted phonon dispersions show excellent agreement, with nearly overlapping curves across the entire Brillouin zone. The MLIP capture the main features of the experimental dispersion, particularly in the acoustic branches, while some discrepancies are observed in the optical branches. Since MLIP cannot exceed DFT-level accuracy, such discrepancy reflects inherent limitations of the underlying DFT reference data. Despite this, the strong agreement in the acoustic regime is encouraging; to provide reasonable prediction of κ_L , as low-frequency acoustic phonons typically dominate lattice thermal conductivity due to their high group velocities and longer lifetimes.

Finally, we evaluated the defect formation energies (E_f) of stoichiometric defects in UN. This serves a critical assessment of the potential to be applied to radiation damage studies of UN as nuclear fuel. The computed values of E_f for bound and unbound U_{FP} , N_{FP} and SD are summarized in Table II, along with corresponding results from previously developed interatomic potentials, and the DFT calculations using the same settings as those employed for database generation. The MTP-predicted defect formation energies are in good agreement with DFT benchmarks. By comparison, a notable discrepancy was observed in the predictions from the Kocevski potential, which significantly overestimates the formation energies of both bound and unbound U_{FP} . This deviation has been previously attributed to deficiencies in the Kocevski potential’s description of metallic uranium, which affect the accuracy of defect energetics in uranium-rich or stoichiometric

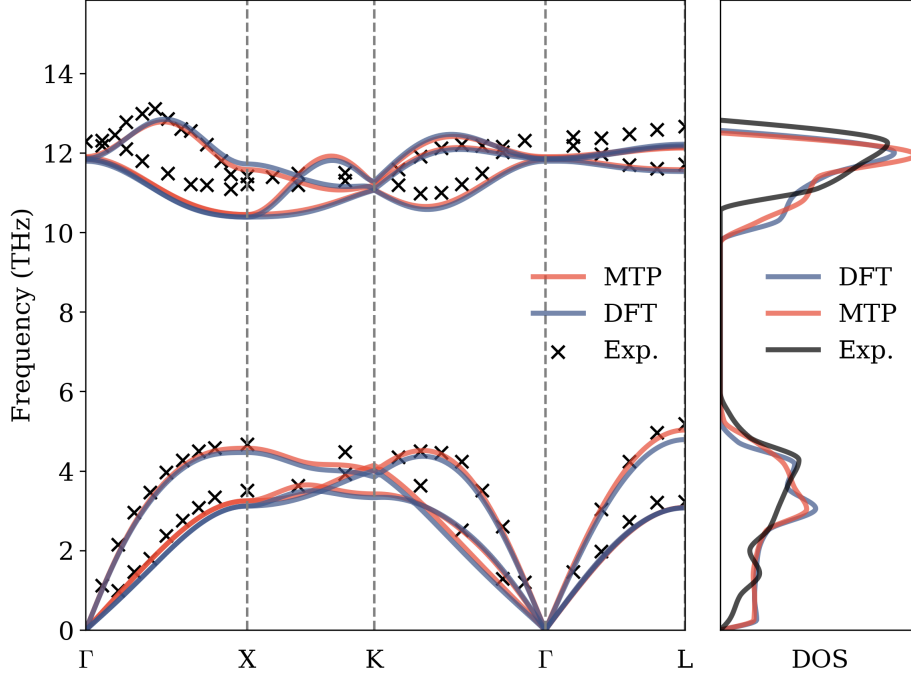


Figure 4. Phonon dispersion and density of state (DOS) of UN predicted by DFT and MTP, compared with the experimental data.

environments²⁸. In contrast, the MTP trained in this work demonstrates improved transferability and accuracy across multiple defect configurations, which supports its suitability for radiation damage modeling in UN.

Defects E_f (eV)	MTP	DFT	Tseplyaev	Kocevski	HIP-NN
unbound U_{FP}	9.04	9.83	9.32	14.41	9.86
bound U_{FP}	8.73	9.04	7.26	10.30	
unbound N_{FP}	4.21	4.59	4.67	4.03	4.99
bound N_{FP}	4.04	4.55	3.76	3.23	
unbound SD	3.88	4.76	4.57	3.98	5.16
bound SD	3.30	4.57	4.51	3.99	4.7

Table II. Formation energies (E_f) of bound and unbound U_{FP} , N_{FP} and Schottky defects predicted by MTP and DFT calculations in this work. Reference values of E_f from the Tseplyaev and Kocevski potentials are taken from AbdulHameed et al.²⁸, while those from the HIP-NN potential are taken from Alzate-Vargas et al.³⁷

C. Thermal properties

1. Thermal expansion

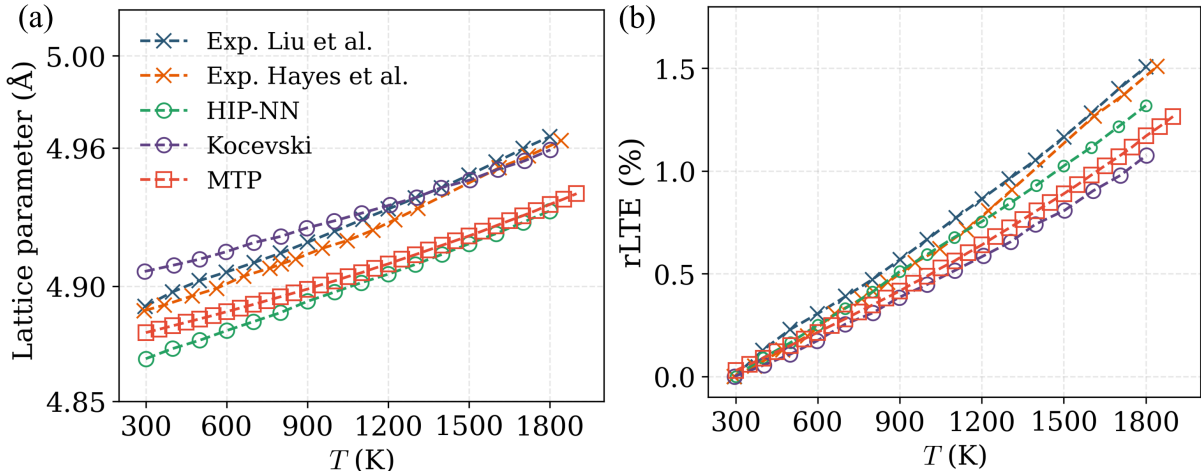


Figure 5. (a) Lattice parameter and (b) relative linear thermal expansion (rLTE in %) as functions of T predicted by MTP, compared with experimental data from Liu et al.⁸ and Hayes et al.¹¹ as well as MD simulation results obtained using the HIP-NN potential³⁷ and the Kocevski potential²⁷.

Thermal expansion is a fundamental property of materials that reflects the anharmonicity of atomic interactions and plays a critical role in applications involving dimension stability and thermal stress. The lattice parameter as a function of temperature is illustrated in Fig. 5a, and the rLTE, calculated using Eq. 4, is presented in Fig. 5b. These results are compared against experimental measurements by Liu et al.⁸ and Hayes et al.¹¹, as well as MD predictions using the HIP-NN potential³⁷ and the empirical Kocevski potential²⁷. The MTP-predicted lattice parameter increases smoothly with temperature and exhibits a thermal expansion trend that closely follows the experimental data. However, a slight overall deviation in the absolute lattice constant was observed across the full temperature range. Both MLIPs (MTP and HIP-NN) yield similar predictions, MTP shows slightly better agreement with experimental values at lower temperatures, while the Kocevski empirical potential shows slightly better agreement with experimental values at high temperatures. Comparing the rLTE values, all potentials yield very consistent values compared to the experiments, although a slight underestimation is observed for all potentials at higher temperatures. Overall, those potentials and experimental measurements demonstrate good consistency in capturing the thermal expansion behavior of UN.

2. Specific heat

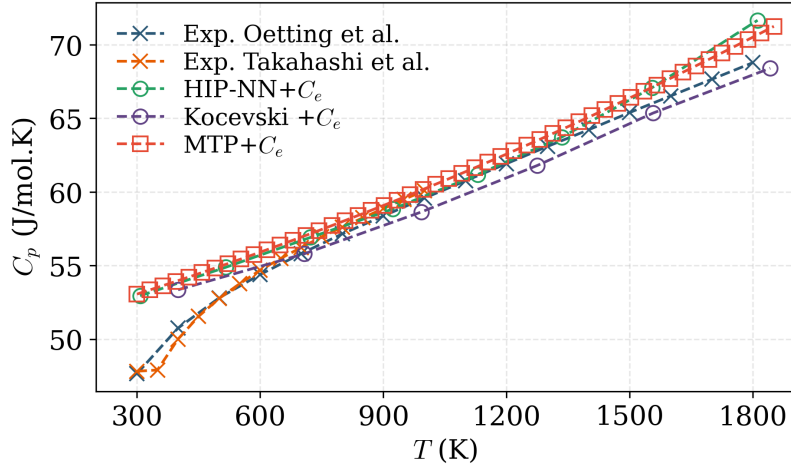


Figure 6. Specific heat of UN with respect to temperature.

In addition to thermal expansion, MD simulations are also employed to calculate the specific heat (C_p) of UN using the developed MTP, under the same conditions as those used for the thermal expansion analysis. The results, presented in Fig. 6, are compared with MD simulation data obtained using the HIP-NN and Kocevski potentials^{28,37}, as well as with experimental measurements reported by Takahashi et al.⁹ and Oetting et al.⁷⁵. Additionally, the electronic contribution to the specific heat of FM UN, calculated from DFT in Ref.¹⁸, is included in all MD results to ensure consistency with experimental data.

At temperatures above 600 K, all three MD-based predictions show excellent mutual consistency and good agreement with experimental data. However, at lower temperatures (below 600 K), a consistent overestimation of specific heat is observed across all three potentials, with the deviation becoming more pronounced as the temperature decreases. This discrepancy is a well-known limitation of classical MD simulations, which inherently include contributions from all phonon modes given their classical treatment of atomic vibrations. The experimental heat capacities at low temperatures are lower compared to predicted results may be due to the fact that many phonon modes, especially high-frequency ones, are not thermally populated due to quantum effects, resulting in lower experimental heat capacities. Because classical MD does not incorporate quantum statistics (e.g., Bose–Einstein distribution), it fails to capture the temperature-dependent suppression of phonon occupation and thus systematically overpredicts specific heat in the low-temperature regime. The Debye temperature for UN is predicted to be around 362 K

as estimated from both experimental and computation by AbdulHameed et al.²⁸, which hints that electron-phonon coupling also have some effect, because the effect of electron-phonon coupling also becomes negligible at 600K, which will be discussed at Section III C 4.

3. Melting Point

Here, the melting point T_m of UN was calculated using MD simulation. The system was incrementally heated from 2600 K to 3600 K within 200 ps, allowing gradual materials response upon increasing temperature. As shown in Fig. 7, the enthalpy as a function of temperature was plotted to identify the onset of melting. The melting point corresponds to a sharp increase in enthalpy, with the latent heat associated with the solid-liquid phase transition. The exact value of T_m is determined by the intersection of the two linear fits (one applied to the solid-phase enthalpy data and the other to the transition region), as shown in Figure 7. From this analysis, T_m is estimated to be approximately 3080 K. This value shows excellent agreement with the experimentally recommended melting point of 3120 ± 30 K⁷⁶ and is also close to the 3150 K predicted using the Kocevski potential²⁸. Hence, this MLIP can be used to reliably capture high-temperature behavior and phase instability.

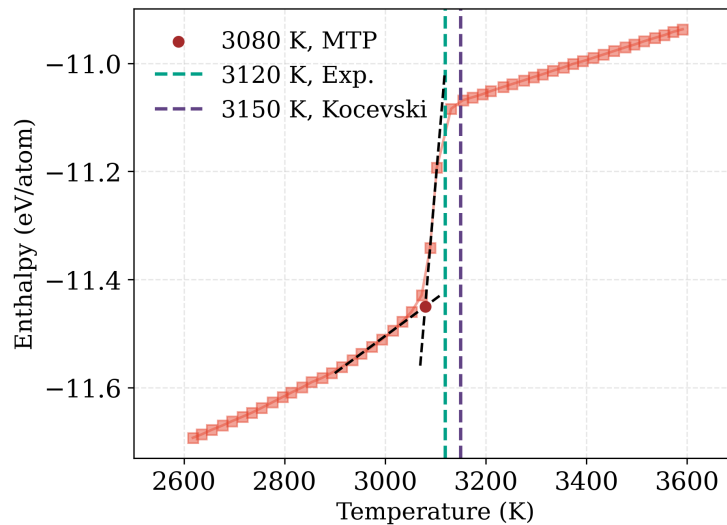


Figure 7. Prediction of the melting point of UN via the enthalpy-temperature relationship using the developed MTP

4. Thermal conductivity

To evaluate how well the developed MTP predicts lattice thermal conductivity (κ_L), we examined how different orders of phonon scattering affect the results. Previous studies include only three-phonon scattering when solving the BTE¹⁸, but recent work in many other systems (e.g.,^{77,78}) has shown that four-phonon scattering can become important, especially at high temperatures. In this work, we considered both three- and four-phonon scattering and directly compare their effects on the thermal conductivity of UN. Figure 8a shows the total lattice thermal conductivity calculated with and without four-phonon scattering. At low temperatures, the effect of four-phonon scattering is negligible, while the impact of four-phonon scattering becomes substantial, leading to a noticeable reduction in κ_L (e.g., 40 % reduction at 900 K in this work). This trend is expected, as higher temperatures increase lattice anharmonicity, which in turn enhances higher-order phonon scattering processes such as four-phonon interactions. To quantify this behavior, Figs. 8c and 8e compare the total phonon scattering rates with and without four-phonon scattering at 77 K and 900 K, respectively. At 77 K, the scattering rates from both cases nearly overlap; in contrast, at 900 K, the inclusion of four-phonon scattering leads to a clear increase in the total scattering rate, particularly for high-frequency modes. To dive into the phonon scattering rates, Figure 8c and 8e compare the phonon scattering rate with and without four phonon scattering for 77 K and 900 K, respectively. It can be seen that the difference in scattering rate is obvious for 900 K while at 77 K, the values almost overlap. This temperature-dependent behavior can be theoretically explained by the scaling of phonon scattering rates with temperature. For phonons of a given frequency, the three-phonon scattering rate scales linearly with temperature ($\tau_{3\text{ph}}^{-1} \propto T$), while the four-phonon scattering rate increases quadratically ($\tau_{4\text{ph}}^{-1} \propto T^2$)⁷⁷. As a result, four-phonon scattering must be included to accurately capture the thermal resistance for high temperature applications.

Due to the metallic nature of UN, electrons play a significant role in thermal transport. In addition to phonon–phonon interactions, electron–phonon scattering serves as an important mechanism that limits κ_L . To quantify this effect, we calculated electron–phonon coupling, which was then incorporated into the phonon scattering rates for evaluating κ_L . Figure 8b compares the lattice thermal conductivity calculated with and without electron–phonon scattering, both on top of the already-included four-phonon scattering. A substantial difference is observed at low temperatures: electron–phonon interactions significantly suppress κ_L (e.g., reducing it by 80% at 77 K).

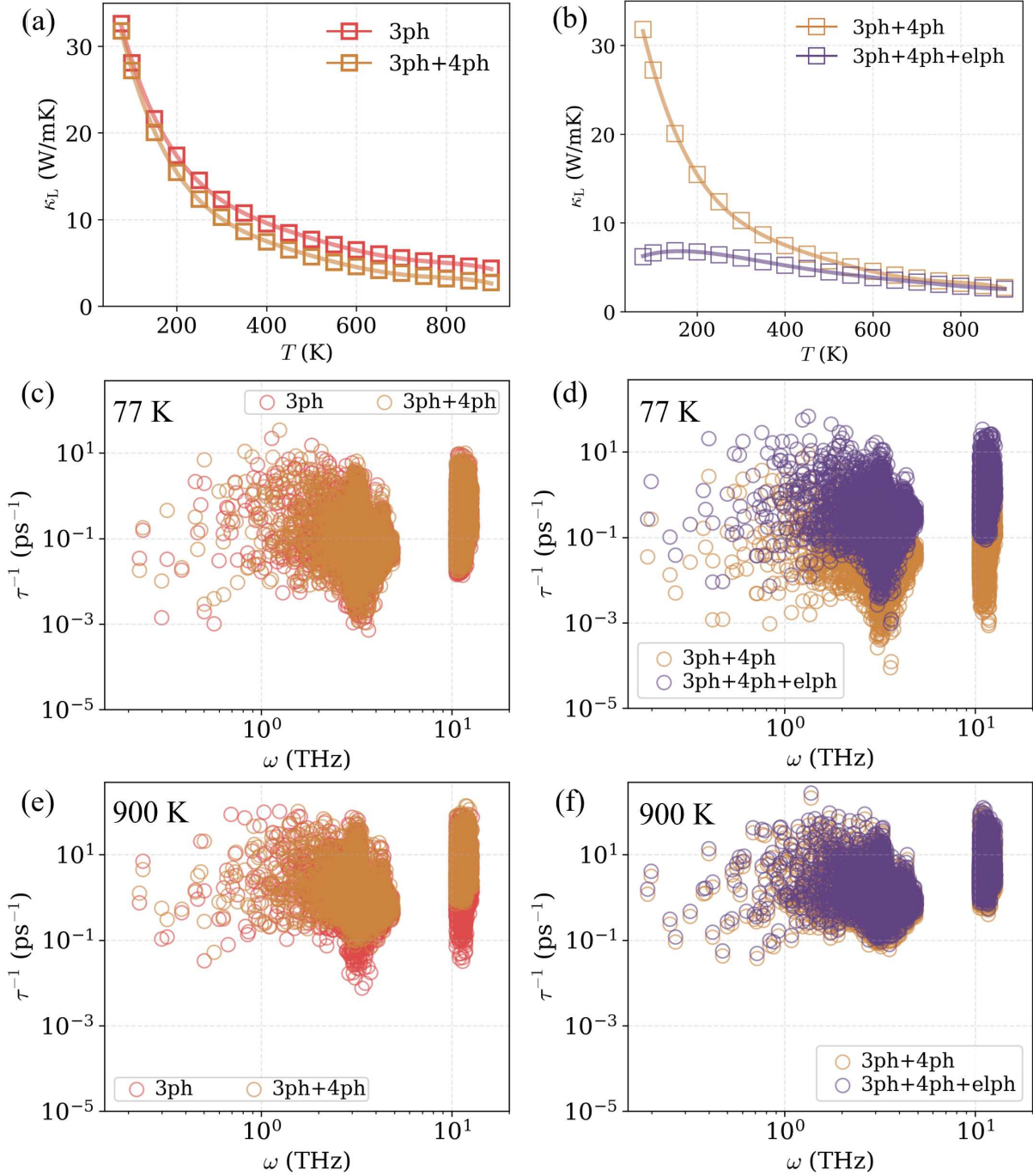


Figure 8. (a) Comparison of lattice thermal conductivity (κ_L) considering only three-phonon scattering and both three-phonon and four-phonon scattering from 77 to 900 K. (b) Effect of electron-phonon scattering on κ_L over the temperature range of 77–900 K. (c) Comparison of phonon scattering rates (τ^{-1}) considering only three-phonon scattering and both three-phonon and four-phonon scattering at 77 K. (d) Effect of electron-phonon scattering on τ^{-1} at 77 K. (e) Comparison of τ^{-1} considering only three-phonon scattering and both three-phonon and four-phonon scattering at 900 K. (f) Effect of electron-phonon scattering on τ^{-1} at 900 K.

However, as temperature increases, the influence of electron–phonon scattering rapidly diminishes ($> \sim 600$ K). This temperature-dependent behavior is consistent with theoretical expectations. At low temperatures, the phonon population is limited to low-frequency modes, which couple more effectively with electrons. As temperature increases, phonon–phonon scattering (especially four-phonon processes) becomes the dominant resistive mechanism, overwhelming the influence of electron–phonon interactions. As a validation, we plot the total phonon scattering rates at 77 K and 900 K in Figs. 8d and 8f, respectively. At 77 K, the inclusion of electron–phonon scattering substantially increases the total phonon scattering rate across the whole frequency range. At 900 K, the scattering rates with and without electron–phonon interactions are nearly identical, confirming that phonon–phonon processes dominate in this regime.

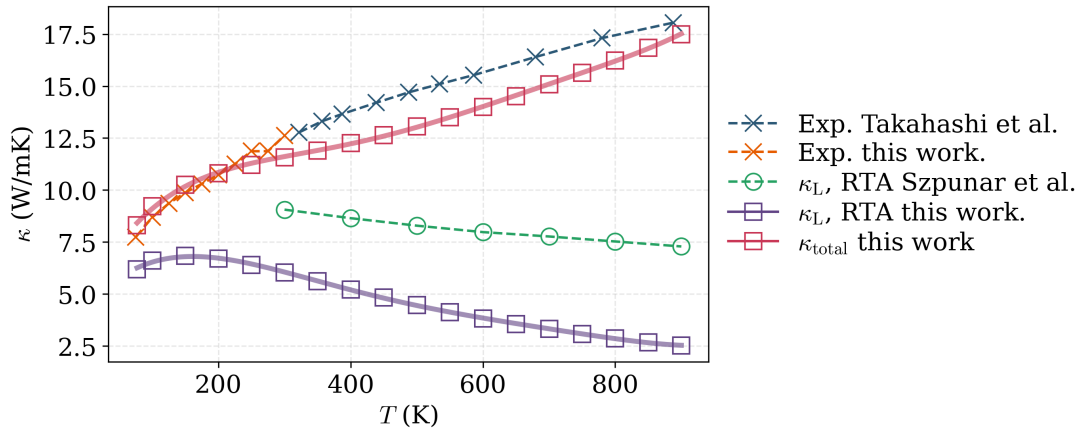


Figure 9. Predicted total thermal conductivity (κ_{total}) compared with experimental data measured in this work below 300 K and with data from Takahashi et al.⁹ κ_{L} from this work, which considers three-phonon, four-phonon, and electron-phonon scattering, is also compared with the results from Szpunar et al.¹⁸, which consider three-phonon scattering.

Given the metallic nature of UN, electrons play a major role in thermal transport, particularly at high temperatures. Here, the total thermal conductivity of UN is evaluated by combining κ_{L} , which accounts for three-phonon, four-phonon, and electron-phonon scattering, with κ_{e} evaluated from Eq 8 and 9. As shown in Fig. 9, the resulting κ_{total} generally shows good agreement with experimental data over a broad temperature range from 77 K to 900 K. The agreement is particularly strong below 300 K. Between 300 K and 800 K, κ_{total} is slightly lower than the experimental values, but the discrepancy diminishes again at temperatures above 800 K. A key contribution of this work is the inclusion of new thermal conductivity measurements using the SDTR technique in

the range of 77 K to 300 K. These measurements address a critical gap in the literature, as existing experimental data, such as those by Takahashi et al.⁹, lack low-temperature measurements. Our new addition fills in the data gap and also provides validation for the computational predictions in the low-temperature regime, where we found lattice thermal conductivity dominates and electron–phonon interactions play a significant role. This comparison with experimental data across the whole temperature range strengthens the reliability of the developed MTP for thermal transport applications.

For further comparison, Fig. 9 also includes lattice thermal conductivity data from Szpunar et al.¹⁸, obtained using RTA based on DFT with three-phonon scattering. While their study offered early insights into phonon transport in UN, their results show some inconsistencies across temperature, likely due to the omission of higher-order scattering processes. The improved agreement observed in our results highlights the importance of including both four-phonon and electron–phonon interactions for a more complete description.

Our findings also clarify the evolving role of phonons and electrons with temperature. Below ~ 300 K, κ_L is the primary contributor to heat transport, but it is significantly reduced by electron–phonon scattering. As temperature increases, phonon–phonon scattering, especially four-phonon processes, further lowers κ_L , while κ_e steadily increases. Above ~ 800 K, electronic transport dominates, consistent with UN’s metallic nature.

IV. CONCLUSION

In this work, a MLIP based on the MTP framework was developed for predicting the thermal properties of UN. The MTP was trained using DFT-generated data and initially validated through the prediction of physical properties, including the equation of state, lattice constant, elastic constants, phonon dispersion, and defect formation energies. These results were benchmarked against DFT calculations, available experimental data, and predictions from other interatomic potentials. Overall, the developed MTP demonstrates balanced performance across a wide range of properties, avoiding the specific biases observed in other potential models.

The validated MTP was then employed to predict the thermal properties of UN, including melting point, thermal expansion, specific heat, and thermal conductivity. The results show good agreement with experimental data. Notably, by incorporating new thermal conductivity measurements on single-crystalline UN, the study emphasizes the significant roles of four-phonon and electron-

phonon scattering processes in accurately capturing thermal conductivity over a broad temperature range. Nevertheless, we also acknowledge that some minor discrepancies between the modeling results and experiments may be attributed to the absence of antiferromagnetic (AFM) ordering in the simulations, which might be better suited for certain properties.

The developed MTP enables MD simulations with quantum-level accuracy at a fraction of the computational cost of traditional DFT methods. This work demonstrates the effectiveness of the developed MLIPs in capturing thermophysical behavior and also lays the groundwork for future studies on defect evolution and radiation effects. Building on this foundation, our next study will focus on how point defects influence heat transport in UN, advancing the understanding of thermal behavior in irradiated UN.

ACKNOWLEDGMENTS

This work is supported by the Center for Thermal Energy Transport under Irradiation, an Energy Frontier Research Center funded by the U.S. Department of Energy, Office of Science, Office of Basic Energy Sciences.

DATA AVAILABILITY

The data that supports the findings of this study are available from the corresponding author upon reasonable request.

REFERENCES

- ¹S.L. Hayes, J.K. Thomas, and K.L. Peddicord. Material property correlations for uranium mononitride: III. transport properties. *Journal of Nuclear Materials*, 171:289–299, 5 1990.
- ²Suzanne Jones, Colin Boxall, Chris Maher, and Robin Taylor. A review of the reprocessability of uranium nitride based fuels. *Progress in Nuclear Energy*, 165:104917, 11 2023.
- ³Gilles J. Youinou and R. Sonat Sen. Impact of accident-tolerant fuels and claddings on the overall fuel cycle: A preliminary systems analysis. *Nuclear Technology*, 188:123–138, 11 2014.
- ⁴Christian Ekberg, Diogo Ribeiro Costa, Marcus Hedberg, and Mikael Jolkkonen. Nitride fuel for Gen IV nuclear power systems. *Journal of Radioanalytical and Nuclear Chemistry*, 318(3):1713–1725, November 2018.

- ⁵J. A. Jackman, T. M. Holden, W. J. L. Buyers, P. de V. DuPlessis, O. Vogt, and J. Genossar. Systematic study of the lattice dynamics of the uranium rocksalt-structure compounds. *Physical Review B*, 33:7144–7153, 5 1986.
- ⁶M. D. Salleh, J. E. MacDonald, G. A. Saunders, and P. De V. Du Plessis. Hydrostatic pressure dependences of elastic constants and vibrational anharmonicity of uranium nitride. *Journal of Materials Science*, 21:2577–2580, 7 1986.
- ⁷S.L. Hayes, J.K. Thomas, and K.L. Peddicord. Material property correlations for uranium mononitride: II. mechanical properties. *Journal of Nuclear Materials*, 171:271–288, 5 1990.
- ⁸Jiatu Liu, Claudia Gasparrini, Joshua T. White, Kyle Johnson, Denise Adorno Lopes, Vanessa K. Peterson, Andrew Studer, Grant J. Griffiths, Gregory R. Lumpkin, Mark R. Wenman, Patrick A. Burr, Elizabeth S. Sooby, and Edward G. Obbard. Thermal expansion and steam oxidation of uranium mononitride analysed via in situ neutron diffraction. *Journal of Nuclear Materials*, 575:154215, 2023.
- ⁹Y. Takahashi, M. Murabayashi, Y. Akimoto, and T. Mukaibo. Uranium mononitride: Heat capacity and thermal conductivity from 298 to 1000 °k. *Journal of Nuclear Materials*, 38:303–308, 3 1971.
- ¹⁰Steven B. Ross, Mohamed S. El-Genk, and R. Bruce Matthews. Thermal conductivity correlation for uranium nitride fuel between 10 and 1923 k. *Journal of Nuclear Materials*, 151:318–326, 2 1988.
- ¹¹S.L. Hayes, J.K. Thomas, and K.L. Peddicord. Material property correlations for uranium mononitride: I. physical properties. *Journal of Nuclear Materials*, 171:262–270, 5 1990.
- ¹²S. L. Hayes, J. K. Thomas, and K. L. Peddicord. Material property correlations for uranium mononitride. iv. thermodynamic properties. *Journal of Nuclear Materials*, 171, 1990.
- ¹³Zachary Miller, Alex Levinsky, Galen Craven, Vedant Mehta, Massimiliano Fratoni, Joshua White, Anders Andersson, Maria Kosmidou, and Adrien Terricabras. Uranium mononitride (UN) handbook. Technical report, Los Alamos National Laboratory (LANL), 9 2024.
- ¹⁴Denis Gryaznov, Eugene Heifets, and Eugene Kotomin. The first-principles treatment of the electron-correlation and spin–orbital effects in uranium mononitride nuclear fuels. *Physical Chemistry Chemical Physics*, 14:4482, 2012.
- ¹⁵R. A. Evarestov, M. V. Losev, A. I. Panin, N. S. Mosyagin, and A. V. Titov. Electronic structure of crystalline uranium nitride: LCAO DFT calculations. *physica status solidi (b)*, 245:114–122, 1 2008.

- ¹⁶Vancho Kocevski, Daniel A. Rehn, Michael W.D. Cooper, and David A. Andersson. First-principles investigation of uranium mononitride (UN): Effect of magnetic ordering, spin-orbit interactions and exchange correlation functional. *Journal of Nuclear Materials*, 559:153401, 2022.
- ¹⁷Zhi-Gang Mei, Marius Stan, and Benjamin Pichler. First-principles study of structural, elastic, electronic, vibrational and thermodynamic properties of UN. *Journal of Nuclear Materials*, 440:63–69, 9 2013.
- ¹⁸Barbara Szpunar, Jayangani I. Ranasinghe, Linu Malakkal, and Jerzy A. Szpunar. First principles investigation of thermal transport of uranium mononitride. *Journal of Physics and Chemistry of Solids*, 146:109636, 11 2020.
- ¹⁹D R Bowler and T Miyazaki. $\mathcal{O}(N)$ methods in electronic structure calculations. *Reports on Progress in Physics*, 75:036503, 3 2012.
- ²⁰A. P. Thompson, L. P. Swiler, C. R. Trott, S. M. Foiles, and G. J. Tucker. Spectral neighbor analysis method for automated generation of quantum-accurate interatomic potentials. *Journal of Computational Physics*, 285:316–330, 3 2015.
- ²¹Ken Kurosaki, Kimihiko Yano, Kazuhiro Yamada, Masayoshi Uno, and Shinsuke Yamanaka. A molecular dynamics study of the heat capacity of uranium mononitride. *Journal of Alloys and Compounds*, 297:1–4, 2 2000.
- ²²Ken Kurosaki, Kimihiko Yano, Kazuhiro Yamada, Masayoshi Uno, and Shinsuke Yamanaka. A molecular dynamics study of the thermal conductivity of uranium mononitride. *Journal of Alloys and Compounds*, 311:305–310, 10 2000.
- ²³P. H. Chen, X. L. Wang, X. C. Lai, G. Li, B. Y. Ao, and Y. Long. Ab initio interionic potentials for UN by multiple lattice inversion. *Journal of Nuclear Materials*, 404:6–8, 9 2010.
- ²⁴Y. Mishin. *Interatomic Potentials for Metals*, pages 459–478. Springer Netherlands, 2005.
- ²⁵A.Yu. Kuksin, S.V. Starikov, D.E. Smirnova, and V.I. Tseplyaev. The diffusion of point defects in uranium mononitride: Combination of DFT and atomistic simulation with novel potential. *Journal of Alloys and Compounds*, 658:385–394, 2 2016.
- ²⁶V. I. Tseplyaev and S. V. Starikov. The atomistic simulation of pressure-induced phase transition in uranium mononitride. *Journal of Nuclear Materials*, 480:7–14, 11 2016.
- ²⁷Vancho Kocevski, Michael W.D. Cooper, Antoine J. Claisse, and David A. Andersson. Development and application of a uranium mononitride (UN) potential: Thermomechanical properties and Xe diffusion. *Journal of Nuclear Materials*, 562:153553, 4 2022.

- ²⁸Mohamed AbdulHameed, Benjamin Beeler, Conor O.T. Galvin, and Michael W.D. Cooper. Assessment of uranium nitride interatomic potentials. *Journal of Nuclear Materials*, page 155247, 6 2024.
- ²⁹Jörg Behler and Michele Parrinello. Generalized neural-network representation of high-dimensional potential-energy surfaces. *Physical Review Letters*, 98:146401, 4 2007.
- ³⁰Jörg Behler. Neural network potential-energy surfaces in chemistry: a tool for large-scale simulations. *Physical Chemistry Chemical Physics*, 13:17930, 10 2011.
- ³¹Albert P. Bartók, Mike C. Payne, Risi Kondor, and Gábor Csányi. Gaussian approximation potentials: The accuracy of quantum mechanics, without the electrons. *Physical Review Letters*, 104:136403, 4 2010.
- ³²Albert P. Bartók, Risi Kondor, and Gábor Csányi. On representing chemical environments. *Physical Review B*, 87:184115, 5 2013.
- ³³Xiang Guo Li, Chongze Hu, Chi Chen, Zhi Deng, Jian Luo, and Shyue Ping Ong. Quantum-accurate spectral neighbor analysis potential models for Ni-Mo binary alloys and fcc metals. *Physical Review B*, 98:094104, 9 2018.
- ³⁴Alexander V. Shapeev. Moment tensor potentials: A class of systematically improvable interatomic potentials. *Multiscale Modeling and Simulation*, 14:1153–1173, 1 2016.
- ³⁵Yunxing Zuo, Chi Chen, Xiangguo Li, Zhi Deng, Yiming Chen, Jörg Behler, Gábor Csányi, Alexander V. Shapeev, Aidan P. Thompson, Mitchell A. Wood, and Shyue Ping Ong. Performance and cost assessment of machine learning interatomic potentials. *The Journal of Physical Chemistry A*, 124(4):731–745, January 2020.
- ³⁶F. Bock, F. Tasnádi, and I. A. Abrikosov. Active learning with moment tensor potentials to predict material properties: Ti_{0.5}Al_{0.5}N at elevated temperature. *Journal of Vacuum Science & Technology A*, 42, 1 2024.
- ³⁷Lorena Alzate-Vargas, Kashi N. Subedi, Nicholas Lubbers, Michael W. D Cooper, Roxanne M. Tutchton, Tammie Gibson, and Richard A. Messerly. Toward machine learning interatomic potentials for modeling uranium mononitride, 2025.
- ³⁸Keivan Esfarjani and Harold T. Stokes. Method to extract anharmonic force constants from first principles calculations. *Physical Review B*, 77:144112, 4 2008.
- ³⁹G. Kresse and J. Furthmüller. Efficient iterative schemes for ab initio total-energy calculations using a plane-wave basis set. *Physical Review B*, 54:11169–11186, 10 1996.

- ⁴⁰G. Kresse and J. Furthmüller. Efficiency of ab-initio total energy calculations for metals and semiconductors using a plane-wave basis set. *Computational Materials Science*, 6:15–50, 7 1996.
- ⁴¹John P. Perdew, Kieron Burke, and Matthias Ernzerhof. Generalized gradient approximation made simple. *Physical Review Letters*, 77:3865–3868, 10 1996.
- ⁴²Antoine Claisse, Marco Klipfel, Niclas Lindbom, Michel Freyss, and Pär Olsson. GGA+U study of uranium mononitride: A comparison of the u-ramping and occupation matrix schemes and incorporation energies of fission products. *Journal of Nuclear Materials*, 478:119–124, 9 2016.
- ⁴³Jian-Hui Lan, Zi-Chen Zhao, Qiong Wu, Yu-Liang Zhao, Zhi-Fang Chai, and Wei-Qun Shi. First-principles DFT+U modeling of defect behaviors in anti-ferromagnetic uranium mononitride. *Journal of Applied Physics*, 114:223516, 12 2013.
- ⁴⁴N A Curry. An investigation of the magnetic structure of uranium nitride by neutron diffraction. *Proceedings of the Physical Society*, 86:1193–1198, 12 1965.
- ⁴⁵Evgeny V. Podryabinkin and Alexander V. Shapeev. Active learning of linearly parametrized interatomic potentials. *Computational Materials Science*, 140:171–180, 2017.
- ⁴⁶Evgeny Podryabinkin, Kamil Garifullin, Alexander Shapeev, and Ivan Novikov. MLIP-3: Active learning on atomic environments with moment tensor potentials. *The Journal of Chemical Physics*, 159, 8 2023.
- ⁴⁷A. P. Thompson, H. M. Aktulga, R. Berger, D. S. Bolintineanu, W. M. Brown, P. S. Crozier, P. J. in 't Veld, A. Kohlmeyer, S. G. Moore, T. D. Nguyen, R. Shan, M. J. Stevens, J. Tranchida, C. Trott, and S. J. Plimpton. LAMMPS - a flexible simulation tool for particle-based materials modeling at the atomic, meso, and continuum scales. *Comp. Phys. Comm.*, 271:108171, 2022.
- ⁴⁸Ivan Novikov. LAMMPS-MLIP-3 interface. <https://gitlab.com/ivannovikov/interface-lammps-mlip-3>.
- ⁴⁹Francis Dominic Murnaghan. The compressibility of media under extreme pressures. *Proceedings of the National Academy of Sciences*, 30(9):244–247, 1944.
- ⁵⁰Michael J Mehl, Barry M Klein, Dimitri A Papaconstantopoulos, et al. First principles calculations of elastic properties of metals. *Intermetallic compounds: principles and practice*, 1:195–210, 1994.
- ⁵¹A. Gueddim, N. Bouarissa, and A. Villesuzanne. Pressure dependence of elastic constants and related parameters for rocksalt MgO. *Computational Materials Science*, 48:490–494, 5 2010.

- ⁵²Atsushi Togo, Laurent Chaput, Terumasa Tadano, and Isao Tanaka. Implementation strategies in phonopy and phono3py. *J. Phys. Condens. Matter*, 35(35):353001, 2023.
- ⁵³Atsushi Togo. First-principles phonon calculations with Phonopy and Phono3py. *J. Phys. Soc. Jpn.*, 92(1):012001, 2023.
- ⁵⁴Shuichi Nosé. A unified formulation of the constant temperature molecular dynamics methods. *The Journal of Chemical Physics*, 81:511–519, 7 1984.
- ⁵⁵William G. Hoover. Canonical dynamics: Equilibrium phase-space distributions. *Physical Review A*, 31:1695, 3 1985.
- ⁵⁶Zherui Han, Xiaolong Yang, Wu Li, Tianli Feng, and Xiulin Ruan. FourPhonon: An extension module to shengbte for computing four-phonon scattering rates and thermal conductivity. *Computer Physics Communications*, 270:108179, 1 2022.
- ⁵⁷Ziqi Guo, Zherui Han, Dudong Feng, Guang Lin, and Xiulin Ruan. Sampling-accelerated first-principles prediction of phonon scattering rates for converged thermal conductivity and radiative properties, 2023.
- ⁵⁸H. Lee, S. Poncé, K. Bushick, S. Hajinazar, J. Lafuente-Bartolome, J. Leveillee, C. Lian, J. Lihm, F. Macheda, H. Mori, H. Paudyal, W.H. Sio, S. Tiwari, M. Zacharias, X. Zhang, Nicola N. Bonini, and E. Kioupakis. Electron–phonon physics from first principles using the EPW code. *npj Computational Materials*, 9:156, 2023.
- ⁵⁹S. Poncé, E.R. Margine, C. Verdi, and F. Giustino. EPW: Electron–phonon coupling, transport and superconducting properties using maximally localized Wannier functions. *Computer Physics Communications*, 209:116 – 133, 2016.
- ⁶⁰Nicola Marzari, Arash A. Mostofi, Jonathan R. Yates, Ivo Souza, and David Vanderbilt. Maximally localized Wannier functions: Theory and applications. *Reviews of Modern Physics*, 84:1419–1475, 10 2012.
- ⁶¹Arash A. Mostofi, Jonathan R. Yates, Giovanni Pizzi, Young-Su Lee, Ivo Souza, David Vanderbilt, and Nicola Marzari. An updated version of Wannier90: A tool for obtaining maximally-localised Wannier functions. *Computer Physics Communications*, 185:2309–2310, 8 2014.
- ⁶²R. Franz and G. Wiedemann. Ueber die wärme-leitungsfähigkeit der metalle. *Annalen der Physik*, 165:497–531, 1 1853.
- ⁶³L. Lorenz. Bestimmung der wärmegrade in absolutem maasse. *Annalen der Physik*, 223:429–452, 1 1872.

- ⁶⁴M. Samsel-Czekala, E. Talik, P. de V. Du Plessis, R. Troć, H. Misiorek, and C. Sułkowski. Electronic structure and magnetic and transport properties of single-crystalline UN. *Physical Review B*, 76:144426, 10 2007.
- ⁶⁵V. J. TENNERY, T. G. GODFREY, and R. A. POTTER. Sintering of UN as a function of temperature and n₂ pressure. *Journal of the American Ceramic Society*, 54:327–331, 7 1971.
- ⁶⁶David H. Hurley, Robert S. Schley, Marat Khafizov, and Brycen L. Wendt. Local measurement of thermal conductivity and diffusivity. *Review of Scientific Instruments*, 86, 12 2015.
- ⁶⁷Zilong Hua, Heng Ban, Marat Khafizov, Robert Schley, Rory Kennedy, and David H. Hurley. Spatially localized measurement of thermal conductivity using a hybrid photothermal technique. *Journal of Applied Physics*, 111, 5 2012.
- ⁶⁸A. Yurgens. Temperature distribution in large bi2212 mesas, May 2010. arXiv:1005.2932.
- ⁶⁹W. Ryan Deskins, Amey Khanolkar, Sanjoy Mazumder, Cody A. Dennett, Kaustubh Bawane, Zilong Hua, Joshua Ferrigno, Lingfeng He, J. Matthew Mann, Marat Khafizov, David H. Hurley, and Anter El-Azab. A combined theoretical-experimental investigation of thermal transport in low-dose irradiated thorium dioxide. *Acta Materialia*, 241:118379, 12 2022.
- ⁷⁰Cody A. Dennett, Zilong Hua, Amey Khanolkar, Tiankai Yao, Phyllis K. Morgan, Timothy A. Prusnick, Narayan Poudel, Aaron French, Krzysztof Gofryk, Lingfeng He, Lin Shao, Marat Khafizov, David B. Turner, J. Matthew Mann, and David H. Hurley. The influence of lattice defects, recombination, and clustering on thermal transport in single crystal thorium dioxide. *APL Materials*, 8:111103, 11 2020.
- ⁷¹Zilong Hua, Tiankai Yao, Amey Khanolkar, Xiixin Ding, Krzysztof Gofryk, Lingfeng He, Michael Benson, and David Hurley. Intragranular thermal transport in U-50Zr. *Journal of Nuclear Materials*, 534:152145, 6 2020.
- ⁷²R Hill. The elastic behaviour of a crystalline aggregate. *Proceedings of the Physical Society. Section A*, 65:349–354, 5 1952.
- ⁷³Orson L. Anderson. A simplified method for calculating the debye temperature from elastic constants. *Journal of Physics and Chemistry of Solids*, 24:909–917, 7 1963.
- ⁷⁴J.A.C. Marples. An X-ray study of the structures of UN, UP, US and USe at cryogenic temperatures. *Journal of Physics and Chemistry of Solids*, 31:2431–2439, 11 1970.
- ⁷⁵Franklin L. Oetting and James M. Leitnaker. The chemical thermodynamic properties of nuclear materials I. uranium mononitride. *The Journal of Chemical Thermodynamics*, 4:199–211, 3 1972.

- ⁷⁶U. Carvajal Nunez, D. Prieur, R. Bohler, and D. Manara. Melting point determination of uranium nitride and uranium plutonium nitride: A laser heating study. *Journal of Nuclear Materials*, 449(1):1–8, 2014.
- ⁷⁷Tianli Feng, Lucas Lindsay, and Xiulin Ruan. Four-phonon scattering significantly reduces intrinsic thermal conductivity of solids. *Physical Review B*, 96:161201, 10 2017.
- ⁷⁸Tianli Feng, Xiaolong Yang, and Xiulin Ruan. Phonon anharmonic frequency shift induced by four-phonon scattering calculated from first principles. *Journal of Applied Physics*, 124, 10 2018.

Supplementary materials for "Towards Accurate Thermal Property Predictions in Uranium Nitride using Machine learning interatomic potential"

Beiha Chen,¹ Zilong Hua,² Jennifer K. Watkins,² Linu Malakkal,² Marat Khafizov,³
David H. Hurley,² and Miaomiao Jin^{1, a)}

¹⁾*Department of Nuclear Engineering, The Pennsylvania State University,
University Park, PA 16802, USA*

²⁾*Idaho National Laboratory, Idaho Falls, ID 83415, USA*

³⁾*Department of Mechanical and Aerospace Engineering, The Ohio State University,
Columbus, OH 43210, USA*

^{a)}Electronic mail: mmjin@psu.edu

I. CONVERGENCE TESTS

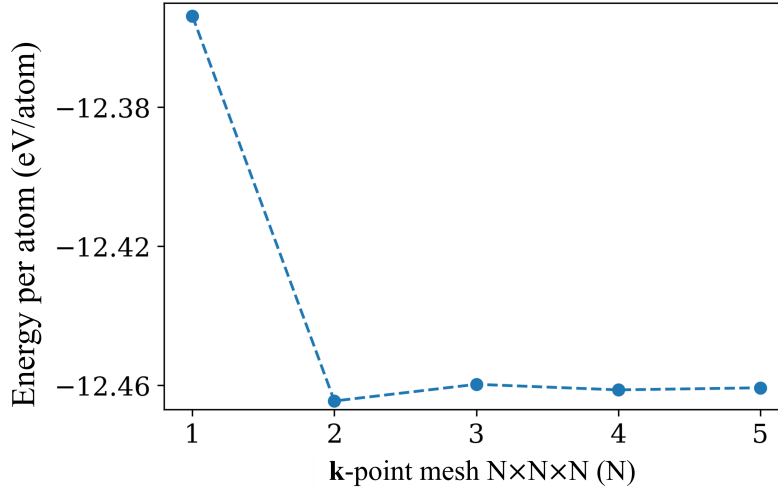


Figure S1. Convergence test of the \mathbf{k} -point mesh in VASP calculations for a $2 \times 2 \times 2$ conventional supercell of uranium nitride (UN), containing 64 atoms. The energy per atom achieves stability at $3 \times 3 \times 3$ \mathbf{k} -point mesh, showing negligible change with further increases in mesh density.

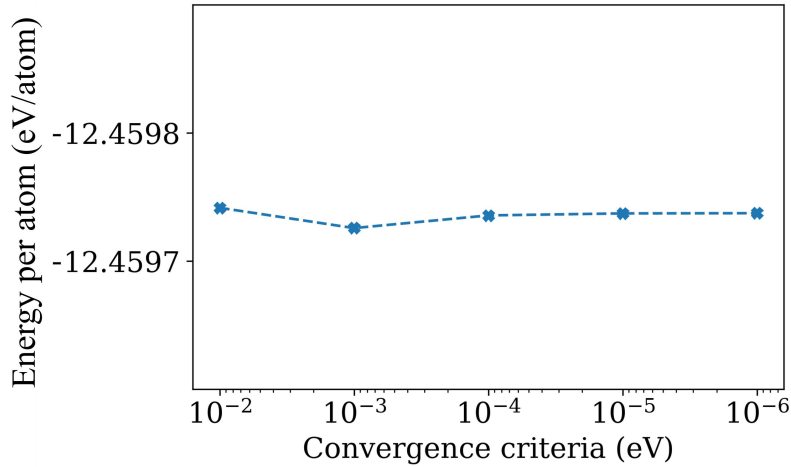


Figure S2. Convergence test of the energy convergence criteria (EDIFF) in VASP calculations for a $2 \times 2 \times 2$ conventional supercell of UN, containing 64 atoms. The energy per atom achieves stability at $\text{EDIFF} = 10^{-4} \text{ eV}$.

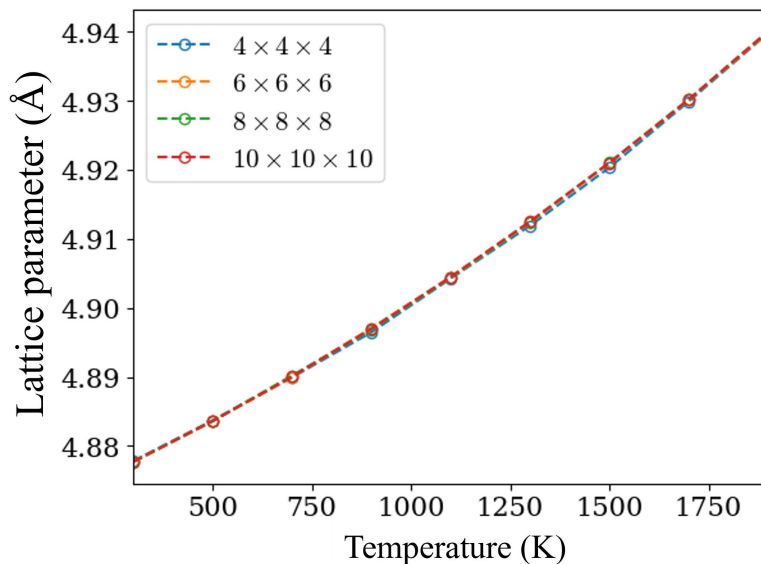


Figure S3. Convergence test of UN conventional supercell sizes for thermal expansion simulation using LAMMPS with the developed MTP. Supercells of sizes $4 \times 4 \times 4$ (512 atoms), $6 \times 6 \times 6$ (1,728 atoms), $8 \times 8 \times 8$ (4,096 atoms), and $10 \times 10 \times 10$ (8,000 atoms) were tested, showing minimal differences in the results.

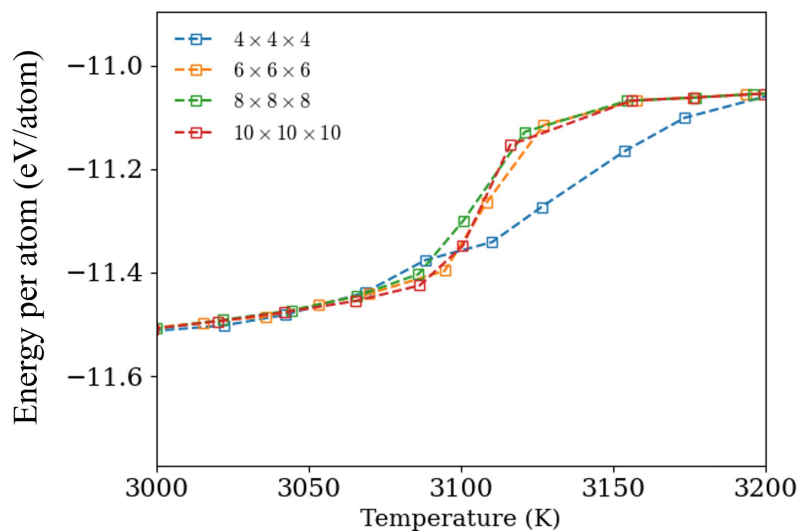


Figure S4. Convergence test of UN conventional supercell sizes for melting simulation using LAMMPS with the developed MTP. Supercells of sizes $4 \times 4 \times 4$ (512 atoms), $6 \times 6 \times 6$ (1,728 atoms), $8 \times 8 \times 8$ (4,096 atoms), and $10 \times 10 \times 10$ (8,000 atoms) were tested. The results show that a $8 \times 8 \times 8$ (4,096 atoms) supercell is sufficient.

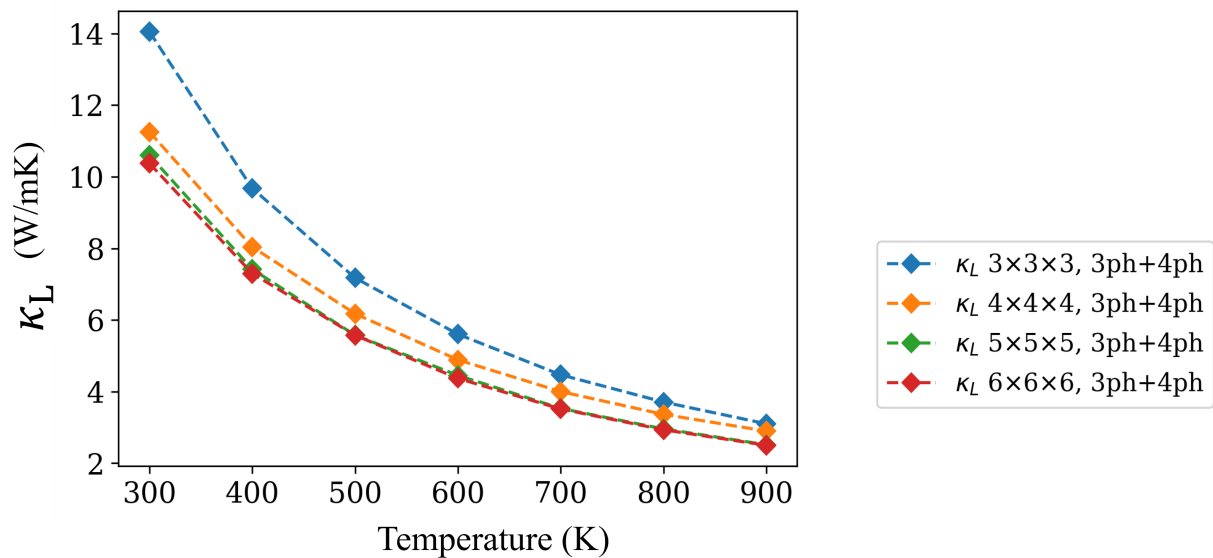


Figure S5. Convergence test of UN primitive supercell sizes for κ_L RTA calculation using ShengBTE with the developed MTP, considering both three-phonon and four-phonon scattering. Primitive supercells of sizes $3 \times 3 \times 3$ (54 atoms), $4 \times 4 \times 4$ (128 atoms), $5 \times 5 \times 5$ (250 atoms), and $6 \times 6 \times 6$ (432 atoms) were tested. The results show that a $5 \times 5 \times 5$ (250 atoms) primitive supercell is sufficient.